Photoluminescent Nano-Patterned Monolayer MoS_2 by Block Copolymer Lithography

Grace G. D. Han[1], Kun-Hua Tu[1], Farnaz Niroui[2], Wenshuo Xu[3], Vladimir Bulovic[2], Caroline A. Ross[1], Jamie H. Warner[3], Jeffrey C. Grossman[1*]

[1]Department of Materials Science and Engineering, Massachusetts Institute of Technology, 77 Massachusetts Avenue, Cambridge, MA, 02139, USA.

[1]Department of Electrical Engineering, Massachusetts Institute of Technology, 77 Massachusetts Avenue, Cambridge, MA, 02139, USA.

[3]Department of Materials, University of Oxford, Parks Road, Oxford, OX1 3PH, United Kingdom

Email: jcg@mit.edu

Abstract

Top-down lithography of large area chemical vapor deposition grown monolayer MoS_2 is achieved using block copolymer patterning and oxygen plasma etching. The MoS_2 nanodots are ~30 nm in diameter and show strong photoluminescence, with a spectral shift compared to the non-patterned MoS_2. The spectral shift of ~15 nm towards higher energy is associated with the release of strain in the monolayer as the lateral dimension is reduced, which is correlated with the Raman mode stiffening. The regular arrays of monodispersed nanodots and nanorods immobilized on a substrate present opportunities in diverse applications including electrocatalysis, sensing, and opto-electronics.

Monolayer transition metal dichalcogenides (TMDs), such as MoS_2 and WS_2, are direct band gap semiconductors and offer new opportunities in electronics, opto-electronics and photonics beyond graphene.[1-3] A key aspect in realizing the potential of 2D materials is the ability to create nanoscale structures with monolayer thickness, using either top-down or bottom-up methods.[4-6] In graphene, nanoribbons have been synthesized by both approaches, with bottom-up growth by the high temperature reaction of molecular based precursors on a substrate [7,8] and the unzipping of carbon nanotubes.[9,10] Chemical exfoliation of bulk MoS_2 has led to the production of small nanoparticles of MoS_2 with modified optical properties. The recent advancements in chemical vapor deposition (CVD) growth of large area 2D TMD monolayer sheets offers an ideal platform for top-down lithography and nanoscale patterning that will be compatible with electronic and opto-electronic applications.

Top-down lithography of 2D materials is often achieved using resist-based electron-beam[11,12] and optical lithography methods,[13] direct patterning by focused ion beams (Ga[14,15] and He[16-18]), energetically preferred chemical etching,[19,20] nanoprobe cutting[21] and block copolymer (BCP) lithography.[22] Block copolymers possessing multiple types of polymer blocks in a backbone are prone to self-assemble into periodic nano-patterns, such as nanodots, nanorods, nanoribbons, and nanomesh,[23] thus enabling nano-lithography of various surfaces of materials including silicon,[24] silicon nitride,[25] metal oxides,[26,27] and so on for the nano-fabrication of air-gap structures, capacitors, field effect transistor, memories, etc.[28] Thin films of BCPs can also play a role in templating the bottom-up growth of nanoparticles and nanowires of TMDs.[29,30] In particular, BCPs have been used to pattern graphene into nanoribbons with sub-10nm width for transistor electronics.[22] Expanding these top-down BCP patterning methods to other 2D materials, such as semiconducting monolayer TMDs, has yet to be achieved.

Here, we use BCP patterning combined with oxygen plasma etching to fabricate nanodots and nanorods in monolayer MoS_2 grown by CVD. A sacrificial interface PMMA layer between the MoS_2 and BCP enables the lift-off of the BCP etch mask after oxygen plasma etching, leaving behind bare MoS_2 nanodots and nanorods. The structures and properties of the MoS_2 film are investigated before and after the lift-off process. Characterization is performed using scanning electron microscopy (SEM), atomic force microscopy (AFM), Raman spectroscopy, and photoluminescence spectroscopy (PL), revealing a significant blue-shift of PL and stiffening of Raman modes attributed to the strain release in the monolayer domains through nano-patterning.

Results

BCP-templated MoS_2 patterning process.

MoS_2 was grown using CVD, with triangular and hexagonal shaped domains on the scale of 10-100 μm randomly distributed across a 1 cm silicon wafer with 300 nm silicon oxide layer. A schematic illustration of the flow-chart process used to create the nanodots in MoS_2 is presented in Figure 1(a). PMMA is first spin-coated over the entire substrate to act as a buffer sacrificial layer for lift-off in the final stages to remove any residual BCP. Next the substrate is coated with a polystyrene-*block*-polydimethylsiloxane (PS-*b*-PDMS) layer which self-assembles into periodic arrays of PDMS particles embedded in a PS matrix through toluene vapor annealing process, as previously reported.[22] PS-*b*-PDMS is chosen for the fabrication of a self-organized nano-template because of its desirable etch selectivity and the formation of highly ordered features due to its high Flory-Huggins interaction parameter (χ).[31]. Oxygen plasma is then used to preferentially etch through the PS region of the BCP and removes the underlying PMMA and MoS_2. The exposure of PDMS to the oxygen plasma results in the conversion to SiO_2 which is immobilized and selectively

covers the underlying PMMA layer and MoS_2. The remaining PMMA and SiO_2 are then removed in a lift-off process by submerging the stack in acetone for at least 4 hours. Figure 1(b) and 1(c) show schematic illustrations of a nano-patterned MoS_2 monolayer domain composed of ~30 nm dots by the BCP-templated lithography.

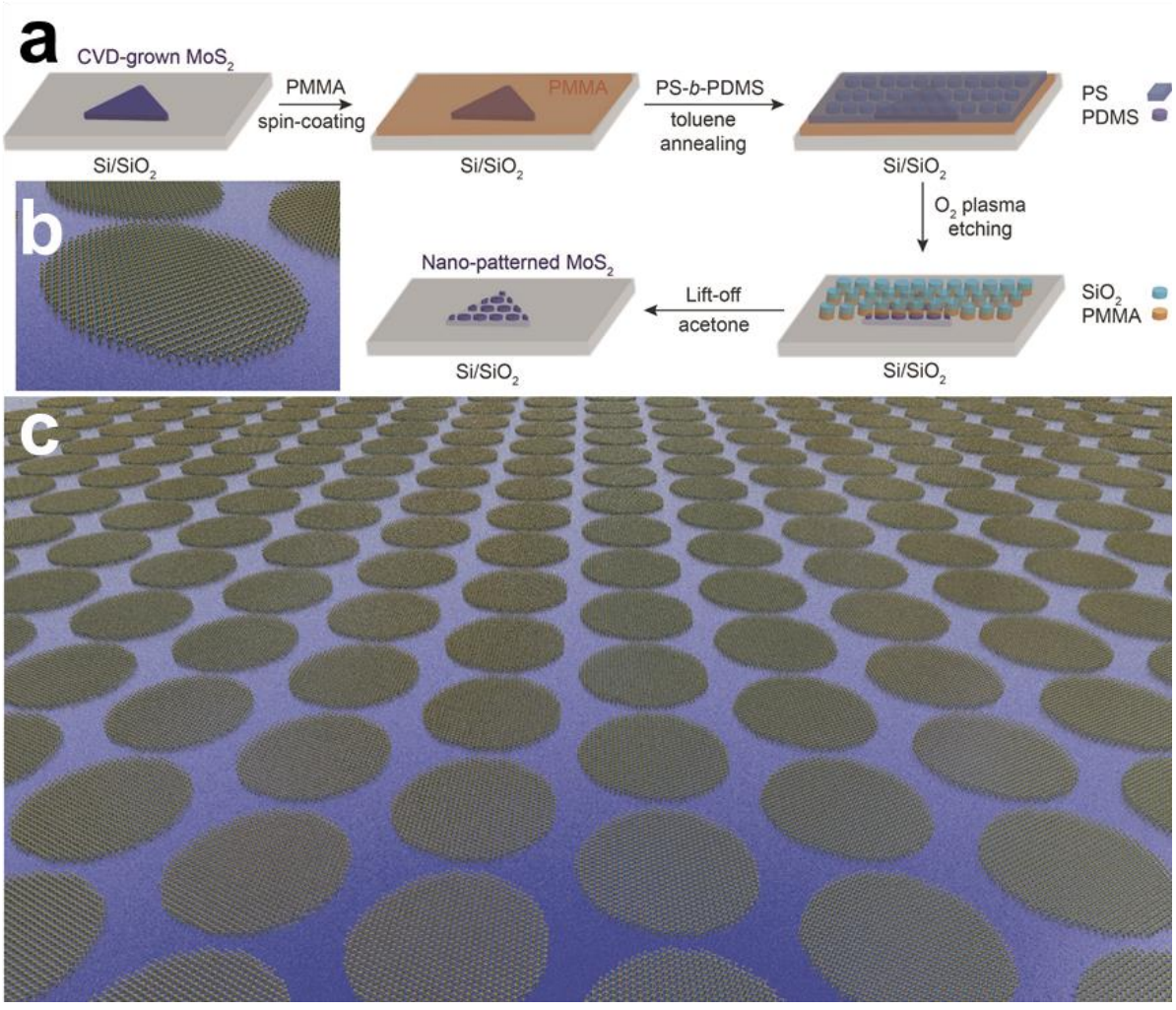

Figure 1. Schematic illustration of the BCP patterning process for nanodot fabrication in MoS_2. (a) Flow chart for nano-patterning procedure of monolayer MoS_2 domains using PS-*b*-PDMS block copolymers as an etch mask. Schematics of (b) monolayer MoS_2 patterned in a shape of dots and (c) an array of nanodots formed as a result of BCP lithography.

The formation of nano-patterned before lift-off of the etch mask was confirmed by SEM as shown in Figure 2. As-grown MoS_2 domains of 10-100 μm scale, which have triangular shapes with uniform contrast (Figure 2(a)), were covered first by a PMMA layer then by a BCP film that generates hexagonally ordered dot arrays of PDMS phase within a thin layer of PS phase. This thin film of the BCP is defined as a monolayer, while any thicker deposition of the BCP, i.e. multilayer of BCP, creates a different phase pattern that resembles the array of rods rather than dots. The patterns of BCP provide an etch mask that replicates the arrangement of PDMS dispersion in the BCP film, and after etching the PDMS regions remain after reacting to form SiO_2, as seen in Figure 2(b–d) with various magnifications. The substrate is completely covered by the pattern, displaying contrast between the areas covered either with SiO_2 rods (appear darker) or dots (lighter), which is clearly seen in Figure 2(d). The phase separation of BCPs creates multilayer defects, and the strategies to achieve more uniform self-assembly of BCPs using directing topographical templates have been investigated.[32] In this work, spontaneous phase separation of PS-*b*-PDMS and the resulting patterns of different shapes were studied, instead of pursuing a uniform patterning strategy.

Figure 2(e) shows coexisting SiO_2 dots and rods with brighter contrast relative to the substrate. The dimensions of the features were analyzed in Figure 2(f) and 2(g) by measuring the line profiles of hexagonally ordered dots and periodically aligned rods. The approximate diameter of the dots appears to be ~30 nm and the width of rods ~25 nm, with a slightly higher packing density of nanorods compared to the nanodots.

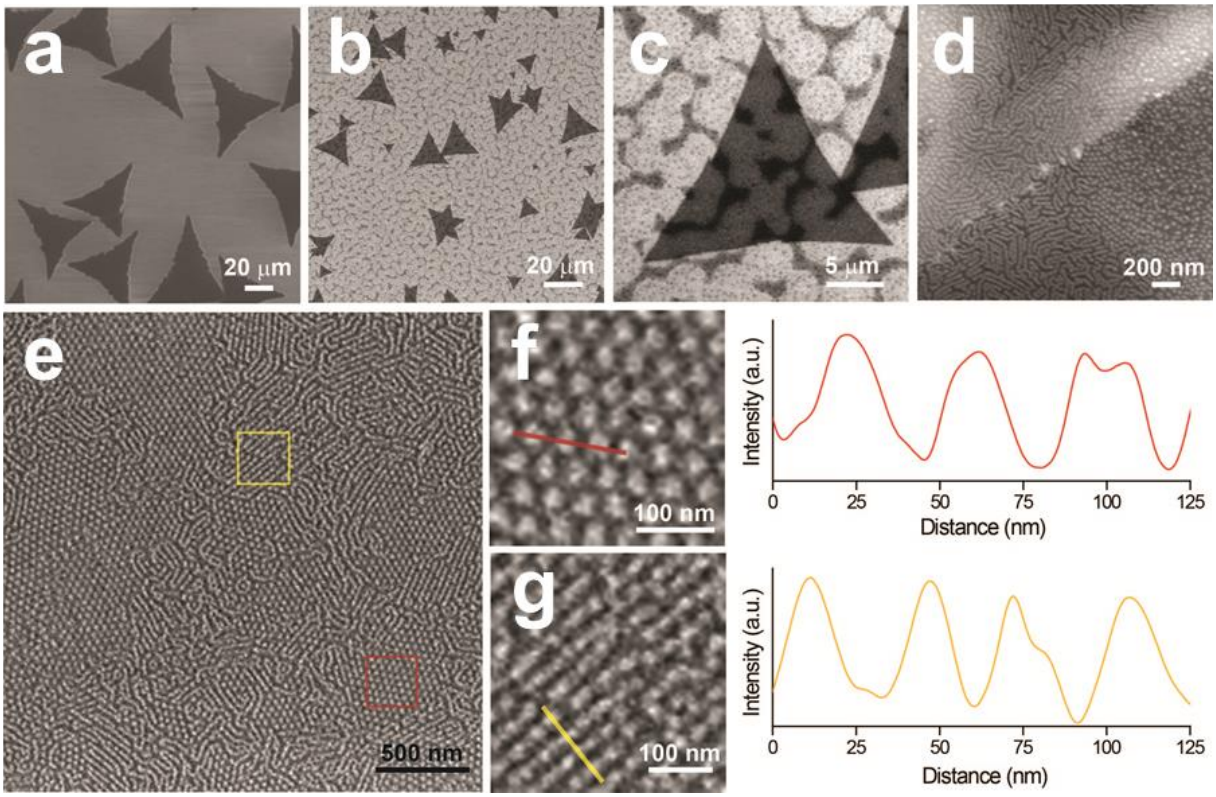

Figure 2. **SEM characterization of the nano-patterned MoS_2 using BCP and oxygen plasma etching.** (a) SEM image of the as-grown MoS_2 before BCP patterning. (b) SEM image showing the large area of the sample covered with SiO_2 nanostructures after oxygen plasma etching of BCP patterns. (c) SEM image of a single triangular MoS_2 domain with SiO_2 pattern. The dark micron-scale patterns represent the areas covered with SiO_2 rods that are generated by the oxidation of BCP multilayer. Lighter regions are covered with SiO_2 dots that are formed by the oxidation of BCP monolayer. (d) SEM image with higher magnification showing the edges of MoS_2 domains (dark contrast) with the SiO_2 mask covering the entire substrate. (e) SEM image of the detailed structure of the SiO_2 mask on MoS_2, showing the presence of well-ordered SiO_2 dot and rod arrays (light contrast). (f) Magnified view of the region indicated with the red box in (e) showing hexagonally packed SiO_2 dots and the line profile of dots. (g) Magnified view of the region

indicated with the yellow box in (e) showing SiO_2 rods and their line profile. The average diameter or width of SiO_2 dots and rods is 25-30 nm.

Next we demonstrate that the nano-patterned monolayer TMDs can remain on the substrate after the removal of the lithographic mask. Figure 3(a) and 3(b) show the optical microscope images of CVD-grown pristine MoS_2 domains and those covered by the SiO_2 after oxygen plasma etching, respectively. The bright micro-scale patterns in Figure 3(b) consist of SiO_2 rods, and the rest of the substrate is instead covered with SiO_2 dots. After lifting off the PMMA sacrificial layer and the overlying SiO_2 by immersing the substrate in acetone, we obtained mainly two types of MoS_2 monolayer domains as in Figure 3(c) and 3(d). The former exhibits mostly unvarying contrast within a domain, similar to a pristine monolayer, whereas the latter displays micro-scale patterns that resemble the arrangement of the SiO_2 mask shown in Figure 3(b) and Figure 2(c). The uniform domains were found near the edges of the substrate where the thick deposition of BCPs leads to the formation of a mask consisting of mainly rods and only a few dots. The domains in Figure 3(d) are present in the center of the substrate where a thin BCP monolayer is formed and produces the mixture of SiO_2 dots and rods after oxygen plasma etching. An SEM image of such domains (Figure 3(e)) exhibits both nanodots and nanorods of monolayer MoS_2, and the measured dimensions of the nano-patterns in Figure 3(f) and 3(g) are consistent with the SiO_2 etched structures in Figure 2. The uniform domains as in Figure 3(c) are composed primarily of rod-shaped structures with on a small number of nanodots interspersed as revealed in by SEM (Figure 3(h)). The ratio of areas covered by dots and rods is determined by the thickness of the deposited BCP and affects the optical contrast of the nano-structured domains. The hexagonally ordered

nanodots form continuous arrays in a large area up to 2 μm in width, Figures 3(e) and 3(i), which confirms the BCP lithographic method for creating nano-structured TMDs.

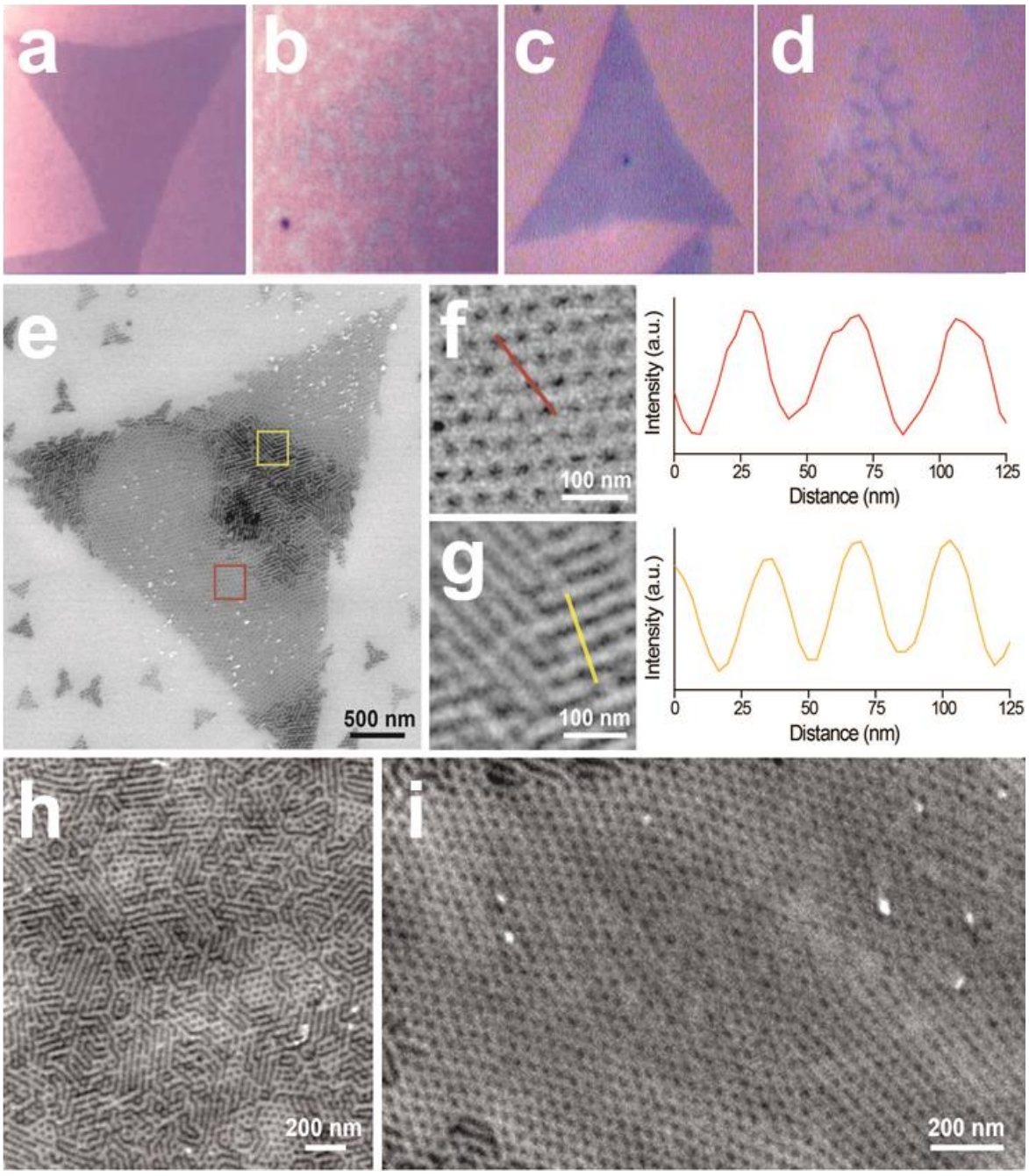

Figure 3. **Optical microscope and SEM characterization of nano-structured MoS_2 after the lift-off process.** Optical microscope images of monolayer MoS_2 domains that are (a) pristine (as-

grown), (b) covered with a SiO_2 mask layer, (c) nano-patterned mostly with rods after the lift-off process, and (d) nano-patterned with dots and rods. (e) SEM image of a nano-patterned monolayer MoS_2 domain comprised of MoS_2 dots and rods, as the domain in (d). (f) Magnified view of the region indicated with the red box in (e) showing hexagonally packed MoS_2 dots and the line profile of dots. (g) Magnified view of the region indicated with the yellow box in (e) showing MoS_2 rods and their line profile. MoS_2 is seen darker relative to the SiO_2 substrate. The average diameter or width of MoS_2 dots and rods is 25-30 nm. (h) A domain patterned mainly in the shape of rods with smaller number of dots filling the space between rods, corresponding to the optical image (c). (i) Larger area of MoS_2 nanodot arrays with a hexagonal order. Bright dots represent SiO_2 mask impurities that remained after the lift-off process.

AFM topography in Figure 4 corroborates the results shown in Figure 3. We probed nano-structured MoS_2 domains and SiO_2 impurities that were partially left behind after the lift-off process (Figure 4(a)). The center of the micro-scale domain was examined in higher magnification where coexisting nanodots and nanorods were found (Figure 4(b)). The height profile across the step edge of the MoS_2 domain on the substrate indicates the monolayer thickness (Figure 4(c)). The magnified regions from Figure 4(b) show the detailed structures of nanodots (Figure 4(d)) and nanorods (Figure 4(e)) that are well defined on the substrate. High-magnification topography of a region within the micro-domain in Figure 4(a) is shown in Figure 4(f) which illustrates both dot- and rod-shaped MoS_2 structures, and their height profiles confirm they are monolayer thickness. The profiles depict round surfaces of the nano-structures rather than flat surfaces with sharp edges, inferring the presence of tip artifact or the non-uniform degrees of O_2 plasma etching on the MoS_2 monolayer along the z-direction (normal to surface).

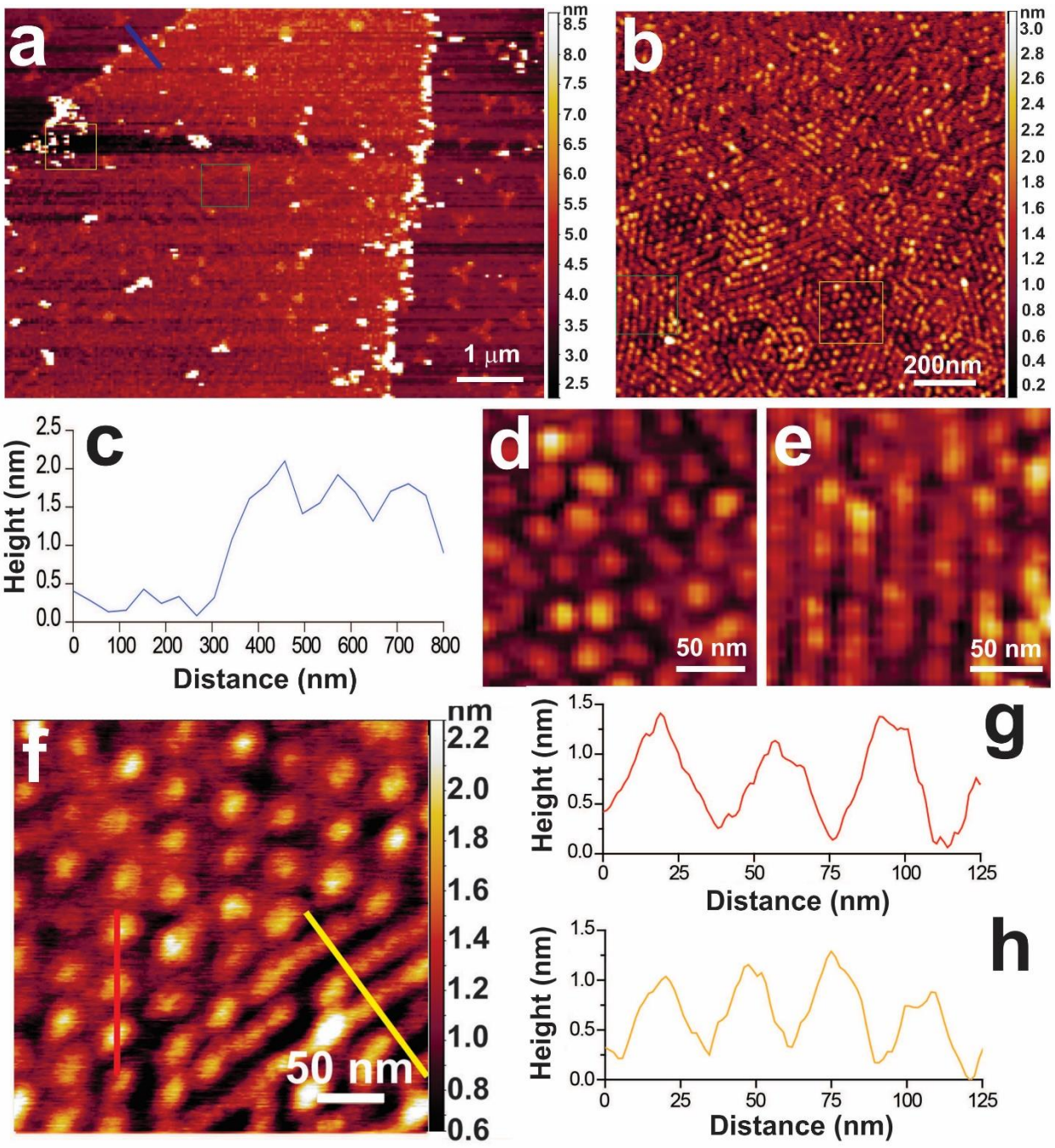

Figure 4. **AFM characterization of nano-structured MoS_2 after the lift-off process.** (a) Low-magnification AFM topography of nano-patterned monolayer MoS_2. (b) Representative mid-magnification topography of the outlined area in (a) (green) in the center of the MoS_2 domain. (c) Height profile of the denoted section (blue line) in (a) proving the monolayer thickness of MoS_2

on SiO_2 substrate. (d) Magnified view of the region indicated with the yellow box in (b) showing nanodots. (e) Magnified view of the region indicated with the green box in (b) showing nanorods. (f) Representative high-resolution topography of the outlined area in (a) (yellow) near the edge of the MoS_2 domain, showing individual MoS_2 dots and rods. Height profiles from the respective red and yellow lines indicated in (f) for (g) nanodots and (h) nanorods. The average height of ~1 nm corresponds to a monolayer thickness, and the average size of the nano-patterns of 25-30 nm matches the SEM characterization.

Optical properties of the nano-structured MoS_2 were investigated by photoluminescence (PL) measurements on the selected spots of ~1 μm size within MoS_2 domains. As-grown pristine MoS_2 domains and those covered by a PMMA layer exhibit identical PL spectra with a peak at 678 nm upon the excitation at 514.5 nm (Figure 5(a)), suggesting the negligible effect of PMMA coating on the photoluminescence of MoS_2 flakes. The parts within the domains covered with SiO_2 dot etch masks show a blue-shifted PL at 663 nm and those with SiO_2 rods behave similarly emitting PL at 666 nm. The shift of 12-15 nm can be attributed to the release of the built-in strain in the monolayer MoS_2 that comes from the rapid cooling after the CVD growth process,[33] also supported by the Raman spectroscopy. Figure 5(b) shows the Raman spectra of pristine and the nano-structured MoS_2. E^1_{2g} and A_{1g} peaks correspond to the in-plane and out-of-plane vibration modes.[34] The pristine MoS_2 shows characteristic peaks at 385 cm^{-1} and 406 cm^{-1}, respectively, and the spacing between two peaks of 21 cm^{-1} agrees with the frequency difference measured in high-quality monolayers as previously reported.[35] As the monolayer is nano-patterned, both characteristic vibration peaks are blue-shifted by 1-2 cm^{-1} for E^1_{2g} mode and 1-4 cm^{-1} for A_{1g} mode, while the frequency difference between two peaks decrease by 1 cm^{-1} for nanorods but increase

by 3 cm^{-1} for nanodots. The stiffening of E^1_{2g} mode in a similar degree has been reported for monolayer MoS_2 domains transferred onto other substrates (SiO_2/Si or h-BN)[36] through a two-step PMMA-assisted process that releases biaxial lattice tensile strain present in the MoS_2 domains directly grown on SiO_2.

After the lift-off of a PMMA layer and a SiO_2 etch mask, the PL and Raman spectra of nano-structured MoS_2 were measured and compared to those of pristine domains. The degree of the blue-shift in PL of ~15 nm resulting from the nano-patterning was similar to that seen before the lift-off process, indicating the marginal effect of a PMMA layer or a SiO_2 mask on the PL measurement (Figure 5(c)). The stiffening of E^1_{2g} and A_{1g} modes by 1.5-2.5 cm^{-1} and 0.5-1 cm^{-1}, respectively, was observed for respective dots and rods in Figure 5(d), similar to the blue-shift with nanorods before the lift-off (Figure 5(b)). As a control experiment, the PMMA-assisted transfer of MoS_2 pristine domains onto another SiO_2/Si substrate was conducted, and E^1_{2g} and A_{1g} peaks at 387 cm^{-1} and 406.5 cm^{-1} were observed on the transferred MoS_2. The Raman shift of two modes overlaps with the other spectra measured from nano-structures, confirming the correlation between the release of strain and the Raman stiffening. Also, the relative intensity of two modes (A_{1g}/E^1_{2g}) increases in a similar degree for the transferred pristine MoS_2 and for the nano-structured domains.

Since the stiffening of both E^1_{2g} and A_{1g} modes after the lift-off appears consistent regardless of the dimension of the MoS_2 domains, the more significant A_{1g} blue-shift of the nanodots before the lift-off (Figure 5(b)) implies the doping level change or the stronger interaction with the PMMA layer compared to that of other structures. The strong binding of nanodots to PMMA layer and relatively loose attachment onto SiO_2 substrate has been observed during longer

lift-off processes where the nanodots were found detached from the substrate as opposed to the remaining nanorods and the unpatterned pristine MoS_2 flakes (Supplementary Figure x).

The relative PL intensities of as-grown and nano-patterned MoS_2 domains are plotted by normalizing to the Raman A_{1g} mode intensity of each sample, which eliminates other factors from the comparison such as materials quantity, excitation intensity, and local electric field.[2] The Raman intensity and shift of A_{1g} mode are reported to be more consistent compared to E^1_{2g} mode with respect to varied density of sulfur vacancy.[37] Figure 5(e) shows that the PL efficiency of nanodots and nanorods is decreased to 13% and 42% of the pristine monolayer respectively, which is attributed to the increased defect trapping rate in the nano-structured domains carrying higher edge-to-area ratio. Edge region is presumed to be more disordered than the crystalline interior and to have lower exciton emission intensity due to the increased quenching.[38] Time-resolved PL experiments were performed on pristine and nanorod MoS_2 domains, while the MoS_2 nanodots were difficult to measure accurately due to their lower relative PL intensity. The room temperature PL decay from the nanorods was nearly identical to the pristine domain, Figure 5(f), with some convolution from the instrument response function. The PL decay time constant of ~1 ns agrees with the previous experimentally and theoretically obtained values.[39,40]

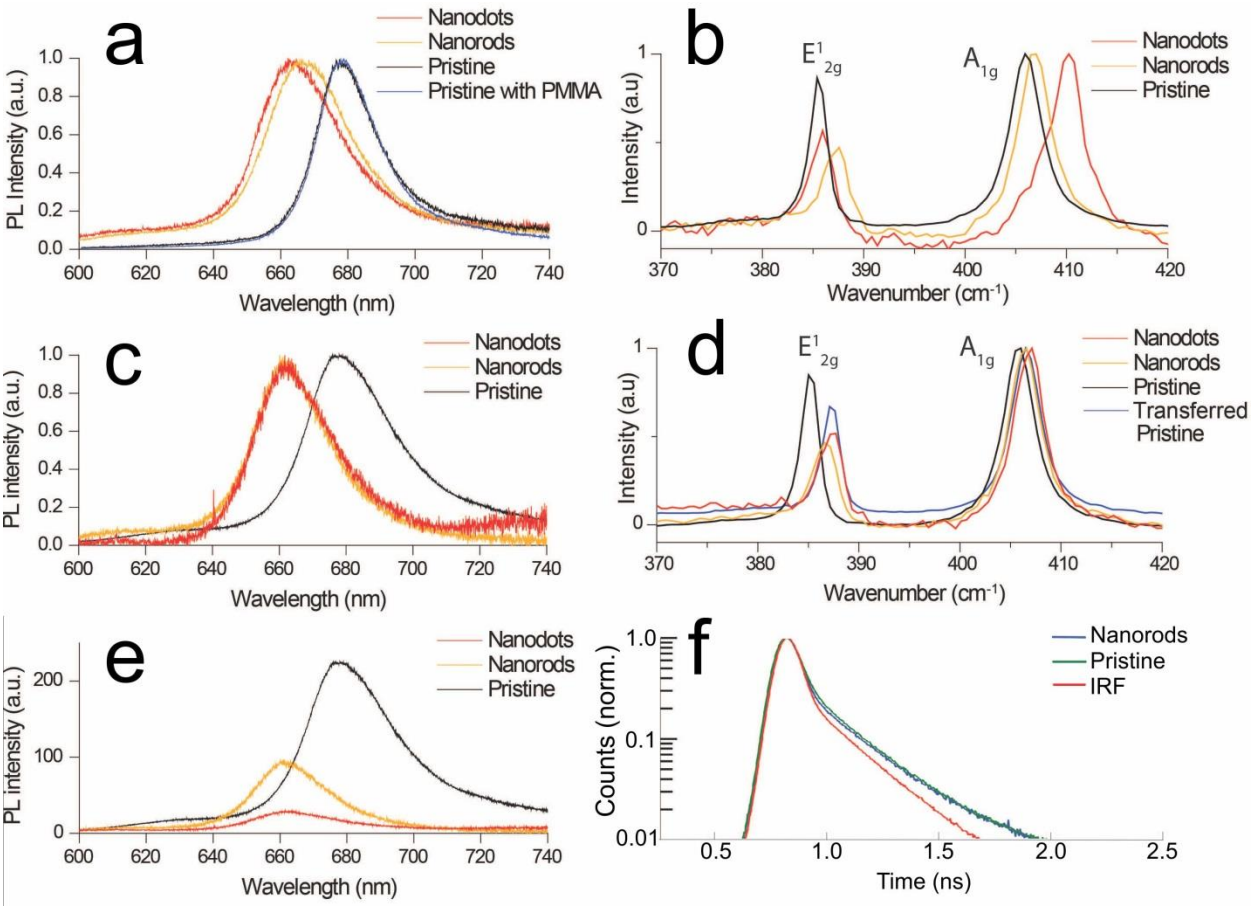

Figure 5. Normalized photoluminescence (PL) (a) and Raman (b) spectra of monolayer MoS_2 nanodots and nanorods before the lift-off process (under a SiO_2 mask after O_2 plasma etching) and those of pristine MoS_2 shown for comparison. Normalized PL (c) and Raman (d) spectra of monolayer MoS_2 nanodots and nanorods after the lift-off process and those of as-grown MoS_2 domains included for comparison. The Raman spectra of pristine domains transferred onto another SiO_2 substrate exhibits similar shifts of both E^1_{2g} and A_{1g} modes to those of nano-patterns. (e) Relative PL of nano-patterned and pristine domains after the lift-off process (identical data as shown in (c)). (f) Transient PL spectra of nanorods and pristine MoS_2 relative to IRF (instrument response function).

Discussion

Although monolayer TMD dots in nano-scale have been synthesized by chemical exfoliation with intense sonication of bulk materials,[5,41-43] the unambiguous understanding of the size-dependent properties of these dots remain a challenge due to the structural deformation and the polydispersity in dimensions.[44] Our method of nano-lithography employing periodic PS-*b*-PDMS BCP templates can generate ordered micron scale arrays of monodispersed nanodots in continuous areas and also nanorods in a predictable way. The uniform size and distribution of nano-patterns were directly monitored by SEM and AFM, and the consistent shift of their optical properties was successfully correlated to the strain release across the nano-domains. The lateral dimension of the current nano-structures (25-30 nm) can be further reduced by high temperature oxidation and chemical oxidative reactions which will be the focus of future studies. Lateral size reduction of the nanodots and nanorods will be conducted to create sub-10 nm quantum dots that could display 2D quantum confined excitonic properties. The optical enhancement and the charge transport in the sub-10 nm TMD monolayers will be investigated.

As nanoscale TMD crystals have been incorporated in biosensing of analytes including glucose[45] and DNA,[4] the solution of the uniform nanodots and nanorods, separated by size-dependent filtration or centrifugation, will be utilized for such applications. Moreover, higher catalytic activities of the nano-structured MoS_2 on the electrochemical hydrogen evolution reaction (HER)[46,47] are expected due to the increased edge states that are chemically more active. Further development of nano-patterning TMDs in diverse structures and dimensions by the BCP-assisted nano-lithography will offer tremendous opportunities by utilizing quantum confinement, increased defects, and the edge effects.

Methods

Chemical vapor deposition growth of monolayer MoS_2.

MoS_2 single layers were prepared using a similar approach to that previously reported. [cite] Molybdenum trioxide (MoO_3, ≥99.5%, Sigma-Aldrich) and sulphur (S, ≥99.5%, Sigma-Aldrich) powder were used to grow monolayer MoS_2 on a SiO_2/Si substrate (300 nm thick SiO_2) by chemical vapor deposition (CVD) at atmospheric pressure. Two furnaces were used to enable temperature control on both the precursors and the substrate. The heating temperatures for S, MoO_3 and SiO_2/Si substrate were ~ 180, ~300, and ~800 ^{0}C, respectively, with argon used as the carrier gas. To avoid cross-contamination between MoO_3 and S, MoO_3 powder was placed in an inner tube having a smaller diameter, which was then inserted into the larger 1-inch quartz tube. The S powder was loaded in the outer quartz tube.

Block copolymer patterning and oxygen plasma etching process.

Measurement of PL and Raman spectra.

PL and Raman spectra were acquired using a Horiba LabRAM 800 HR spectrometer equipped with an Ar^+ (514.5 nm) excitation source and a Peltier-cooled CCD detector. The laser was focused on the sample with a 400 nm confocal hole using the 100x objective under reflected illumination. The laser spot on the sample was ~1 μm in diameter and had a power of ~4 mW at the sample surface.

Data availability. The data that support the findings of this study are available from the corresponding author upon request.

References

1 Mak, K. F., Lee, C., Hone, J., Shan, J. & Heinz, T. F. Atomically Thin ${\mathrm{MoS}}_{2}$: A New Direct-Gap Semiconductor. *Phys Rev Lett* **105**, 136805 (2010).

2 Splendiani, A. *et al.* Emerging Photoluminescence in Monolayer MoS2. *Nano Letters* **10**, 1271-1275, doi:10.1021/nl903868w (2010).

3 Zhao, W. *et al.* Evolution of Electronic Structure in Atomically Thin Sheets of WS2 and WSe2. *ACS Nano* **7**, 791-797, doi:10.1021/nn305275h (2013).

4 Ha, H. D., Han, D. J., Choi, J. S., Park, M. & Seo, T. S. Dual Role of Blue Luminescent MoS2 Quantum Dots in Fluorescence Resonance Energy Transfer Phenomenon. *Small* **10**, 3858-3862, doi:10.1002/smll.201400988 (2014).

5 Zhang, X. *et al.* A Facile and Universal Top-Down Method for Preparation of Monodisperse Transition-Metal Dichalcogenide Nanodots. *Angewandte Chemie International Edition* **54**, 5425-5428, doi:10.1002/anie.201501071 (2015).

6 Huang, H. *et al.* Water-Soluble Monolayer Molybdenum Disulfide Quantum Dots with Upconversion Fluorescence. *Particle & Particle Systems Characterization* **32**, 72-79, doi:10.1002/ppsc.201400101 (2015).

7 Cai, J. *et al.* Graphene nanoribbon heterojunctions. *Nat Nano* **9**, 896-900, doi:10.1038/nnano.2014.184

http://www.nature.com/nnano/journal/v9/n11/abs/nnano.2014.184.html#supplementary-information (2014).

8 Han, P. *et al.* Bottom-Up Graphene-Nanoribbon Fabrication Reveals Chiral Edges and Enantioselectivity. *ACS Nano* **8**, 9181-9187, doi:10.1021/nn5028642 (2014).

9 Morelos-Gómez, A. *et al.* Clean Nanotube Unzipping by Abrupt Thermal Expansion of Molecular Nitrogen: Graphene Nanoribbons with Atomically Smooth Edges. *ACS Nano* **6**, 2261-2272, doi:10.1021/nn2043252 (2012).

10 Cruz-Silva, R. *et al.* Formation of Nitrogen-Doped Graphene Nanoribbons via Chemical Unzipping. *ACS Nano* **7**, 2192-2204, doi:10.1021/nn305179b (2013).

11 Lin, J. *et al.* Flexible metallic nanowires with self-adaptive contacts to semiconducting transition-metal dichalcogenide monolayers. *Nat Nano* **9**, 436-442, doi:10.1038/nnano.2014.81

http://www.nature.com/nnano/journal/v9/n6/abs/nnano.2014.81.html#supplementary-information (2014).

12 Liu, X. *et al.* Top–down fabrication of sub-nanometre semiconducting nanoribbons derived from molybdenum disulfide sheets. *Nature Communications* **4**, 1776, doi:10.1038/ncomms2803

http://www.nature.com/articles/ncomms2803#supplementary-information (2013).

13 Liu, W. *et al.* Large Scale Pattern Graphene Electrode for High Performance in Transparent Organic Single Crystal Field-Effect Transistors. *ACS Nano* **4**, 3927-3932, doi:10.1021/nn100728p (2010).

14 Celebi, K. *et al.* Ultimate Permeation Across Atomically Thin Porous Graphene. *Science* **344**, 289-292, doi:10.1126/science.1249097 (2014).

15 Liao, Z. *et al.* Lateral damage in graphene carved by high energy focused gallium ion beams. *Applied Physics Letters* **107**, 013108, doi:10.1063/1.4926647 (2015).

16 Fox, D. S. *et al.* Nanopatterning and Electrical Tuning of MoS2 Layers with a Subnanometer Helium Ion Beam. *Nano Letters* **15**, 5307-5313, doi:10.1021/acs.nanolett.5b01673 (2015).
17 Lemme, M. C. *et al.* Etching of Graphene Devices with a Helium Ion Beam. *ACS Nano* **3**, 2674-2676, doi:10.1021/nn900744z (2009).
18 Bell, D. C., Lemme, M. C., Stern, L. A., Williams, J. R. & Marcus, C. M. Precision cutting and patterning of graphene with helium ions. *Nanotechnology* **20**, 455301 (2009).
19 Liu, H., Hoeppener, S. & Schubert, U. S. Site-Specific Chemical Surface Functionalization and Electronic Patterning of Graphene by Electrooxidative Lithography. *ChemPhysChem* **17**, 2863-2871, doi:10.1002/cphc.201600490 (2016).
20 Byun, I.-S. *et al.* Nanoscale Lithography on Monolayer Graphene Using Hydrogenation and Oxidation. *ACS Nano* **5**, 6417-6424, doi:10.1021/nn201601m (2011).
21 Tapaszto, L., Dobrik, G., Lambin, P. & Biro, L. P. Tailoring the atomic structure of graphene nanoribbons by scanning tunnelling microscope lithography. *Nat Nano* **3**, 397-401, doi:http://www.nature.com/nnano/journal/v3/n7/suppinfo/nnano.2008.149_S1.html (2008).
22 Son, J. G. *et al.* Sub-10 nm Graphene Nanoribbon Array Field-Effect Transistors Fabricated by Block Copolymer Lithography. *Advanced Materials* **25**, 4723-4728, doi:10.1002/adma.201300813 (2013).
23 Bates, C. M., Maher, M. J., Janes, D. W., Ellison, C. J. & Willson, C. G. Block Copolymer Lithography. *Macromolecules* **47**, 2-12, doi:10.1021/ma401762n (2014).
24 Gu, X. *et al.* High Aspect Ratio Sub-15 nm Silicon Trenches From Block Copolymer Templates. *Advanced Materials* **24**, 5688-5694, doi:10.1002/adma.201202361 (2012).
25 Park, M., Harrison, C., Chaikin, P. M., Register, R. A. & Adamson, D. H. Block Copolymer Lithography: Periodic Arrays of ~10¹¹ Holes in 1 Square Centimeter. *Science* **276**, 1401-1404, doi:10.1126/science.276.5317.1401 (1997).
26 Kamcev, J. *et al.* Chemically Enhancing Block Copolymers for Block-Selective Synthesis of Self-Assembled Metal Oxide Nanostructures. *ACS Nano* **7**, 339-346, doi:10.1021/nn304122b (2013).
27 Xiong, S. *et al.* Directed Self-Assembly of Triblock Copolymer on Chemical Patterns for Sub-10-nm Nanofabrication via Solvent Annealing. *ACS Nano* **10**, 7855-7865, doi:10.1021/acsnano.6b03667 (2016).
28 Kim, H.-C., Park, S.-M. & Hinsberg, W. D. Block Copolymer Based Nanostructures: Materials, Processes, and Applications to Electronics. *Chemical Reviews* **110**, 146-177, doi:10.1021/cr900159v (2010).
29 Loginova, T. P. *et al.* Molybdenum Sulfide Nanoparticles in Block Copolymer Micelles: Synthesis and Tribological Properties. *Chemistry of Materials* **16**, 2369-2378, doi:10.1021/cm040147f (2004).
30 Wei, W. *et al.* Synthesis of Molybdenum Disulfide Nanowire Arrays Using a Block Copolymer Template. *Chemistry of Materials* **28**, 4017-4023, doi:10.1021/acs.chemmater.6b01453 (2016).
31 Son, J. G., Hannon, A. F., Gotrik, K. W., Alexander-Katz, A. & Ross, C. A. Hierarchical Nanostructures by Sequential Self-Assembly of Styrene-Dimethylsiloxane Block Copolymers of Different Periods. *Advanced Materials* **23**, 634-639, doi:10.1002/adma.201002999 (2011).
32 Jung, Y. S., Chang, J. B., Verploegen, E., Berggren, K. K. & Ross, C. A. A Path to Ultranarrow Patterns Using Self-Assembled Lithography. *Nano Letters* **10**, 1000-1005, doi:10.1021/nl904141r (2010).
33 Conley, H. J. *et al.* Bandgap Engineering of Strained Monolayer and Bilayer MoS2. *Nano Letters* **13**, 3626-3630, doi:10.1021/nl4014748 (2013).
34 Wang, Y., Cong, C., Qiu, C. & Yu, T. Raman Spectroscopy Study of Lattice Vibration and Crystallographic Orientation of Monolayer MoS2 under Uniaxial Strain. *Small* **9**, 2857-2861, doi:10.1002/smll.201202876 (2013).
35 Huang, S. *et al.* Probing the Interlayer Coupling of Twisted Bilayer MoS2 Using Photoluminescence Spectroscopy. *Nano Letters* **14**, 5500-5508, doi:10.1021/nl5014597 (2014).

36 Wang, S., Wang, X. & Warner, J. H. All Chemical Vapor Deposition Growth of MoS2:h-BN Vertical van der Waals Heterostructures. *ACS Nano* **9**, 5246-5254, doi:10.1021/acsnano.5b00655 (2015).
37 Parkin, W. M. *et al.* Raman Shifts in Electron-Irradiated Monolayer MoS2. *ACS Nano* **10**, 4134-4142, doi:10.1021/acsnano.5b07388 (2016).
38 Bao, W. *et al.* Visualizing nanoscale excitonic relaxation properties of disordered edges and grain boundaries in monolayer molybdenum disulfide. *Nature Communications* **6**, 7993, doi:10.1038/ncomms8993

http://www.nature.com/articles/ncomms8993#supplementary-information (2015).
39 Shi, H. *et al.* Exciton Dynamics in Suspended Monolayer and Few-Layer MoS2 2D Crystals. *ACS Nano* **7**, 1072-1080, doi:10.1021/nn303973r (2013).
40 Palummo, M., Bernardi, M. & Grossman, J. C. Exciton Radiative Lifetimes in Two-Dimensional Transition Metal Dichalcogenides. *Nano Letters* **15**, 2794-2800, doi:10.1021/nl503799t (2015).
41 Dai, W. *et al.* Tunable Fabrication of Molybdenum Disulfide Quantum Dots for Intracellular MicroRNA Detection and Multiphoton Bioimaging. *Small* **11**, 4158-4164, doi:10.1002/smll.201500208 (2015).
42 Gopalakrishnan, D., Damien, D. & Shaijumon, M. M. MoS2 Quantum Dot-Interspersed Exfoliated MoS2 Nanosheets. *ACS Nano* **8**, 5297-5303, doi:10.1021/nn501479e (2014).
43 Lin, L. *et al.* Fabrication of Luminescent Monolayered Tungsten Dichalcogenides Quantum Dots with Giant Spin-Valley Coupling. *ACS Nano* **7**, 8214-8223, doi:10.1021/nn403682r (2013).
44 Jin, H. *et al.* Colloidal Single-Layer Quantum Dots with Lateral Confinement Effects on 2D Exciton. *Journal of the American Chemical Society* **138**, 13253-13259, doi:10.1021/jacs.6b06972 (2016).
45 Ou, J. Z. *et al.* Ion-Driven Photoluminescence Modulation of Quasi-Two-Dimensional MoS2 Nanoflakes for Applications in Biological Systems. *Nano Letters* **14**, 857-863, doi:10.1021/nl4042356 (2014).
46 Jaramillo, T. F. *et al.* Identification of Active Edge Sites for Electrochemical H₂ Evolution from MoS₂ Nanocatalysts. *Science* **317**, 100-102, doi:10.1126/science.1141483 (2007).
47 Li, S. *et al.* Edge-Enriched 2D MoS2 Thin Films Grown by Chemical Vapor Deposition for Enhanced Catalytic Performance. *ACS Catalysis* **7**, 877-886, doi:10.1021/acscatal.6b02663 (2017).

Acknowledgements

Author contributions